

Array Current Reconstruction by Surface Wave Measurements. Two-Dimensional Approximation

E. A. Rudenchik, L. B. Volkomirskaya*, and A. E. Reznikov

*Pushkov Institute of Terrestrial Magnetism, Ionosphere, and Radio Wave Propagation,
Russian Academy of Sciences, Troitsk, Moscow oblast, 142190 Russia;
ZAO Taimer, ul. Solnechnaya 12, Troitsk, Moscow oblast, 142190 Russia*

Received August 25, 2007

Abstract—The dependencies of the array current on the underlying surface properties were studied in the two-dimensional approximation. The results of the array current reconstruction were compared with experimental data of georadar sounding, obtained on the water basin surface. An array current reconstruction algorithm most adequately consistent with experimental data was obtained.

PACS numbers : 43.60.Pt, 77.22.Ch, 84.40.Xb, 91.25.Qi

DOI: 10.3103/S1541308X08030011

INTRODUCTION

The use of the georadar poses problems of instrument calibration and the study of the dependence of the array current on the underlying surface properties. These problems can be solved provided that surface layer properties are well known and it is known how to solve the direct sounding problem. The simplest case is a homogeneous medium; there are no reflected signals, and the measured value is the surface wave. To solve the direct problem, at least the two-dimensional model should be used. In principle, the array current can be reconstructed by measurements at a single specified distance between the transmitter and receiver. Measurements at various distances yield supplementary information which can be used for calibration.

In this paper, algorithms for solving the problem of array current reconstruction are considered on the basis of the two-dimensional approximation and the calculation results are compared with the experimental data obtained using a GROT-10 georadar during a basin investigation.

1. MAXWELL EQUATIONS FOR THE TWO-DIMENSIONAL PROBLEM

An initial point in this analysis is the classical system

$$\begin{aligned} \operatorname{div} \mathbf{D} &= 0, & \operatorname{div} \mathbf{B} &= 0, \\ \operatorname{rot} \mathbf{E} &= -\partial \mathbf{B} / \partial t, & \operatorname{rot} \mathbf{H} &= \partial \mathbf{D} / \partial t + 4\pi \mathbf{J}, \end{aligned}$$

*E-mail: mila@izmiran.ru

$$\mathbf{D}(t) = \mathbf{E}(t) + \int_0^{\infty} f(\tau) \mathbf{E}(t - \tau) d\tau, \quad \mathbf{B} = \mathbf{H}.$$

Let us direct the x , y , and z axes downward, rightward, and against us, respectively. Let the extrinsic current density vector \mathbf{J} be directed along the z axis and medium parameters and J be independent of z . Let us seek solutions generated only by the extrinsic current, i.e., let there be no external signals. Then the electric field E is representable in the form

$$\mathbf{E} = \{0, 0, E(t, x, y)\}, \quad (1.1)$$

$$E(t, x, y) = \frac{1}{2\pi i} \int_{C(x, y)} e^{pt} E(p, x, y) dp, \quad (1.2)$$

$$\begin{aligned} E(p, x, y) &= 4\pi p \int G(p, x, x_0, y - y_0) \\ &\quad \times J(p, x_0, y_0) dx_0 dy_0, \end{aligned} \quad (1.3)$$

$$J(p, x, y) = \int_0^{\infty} e^{-pt} J(t, x, y) dt, \quad (1.4)$$

where $C(x, y)$ is the contour enclosing all of the singularities of the analytical function $E(p, x, y)$, which are arranged in the left halfplane of the complex argument p , and $G(p, x, x_0, y)$ is the Green's function of a plane-layered medium. Let the medium consist of two homogeneous layers and its permittivity be given by

$$\epsilon(p, x) = \begin{cases} \epsilon_a(p), & x < 0, \\ \epsilon_b(p), & x > 0. \end{cases} \quad (1.5)$$

Let the array be an infinitely thin conductor arranged at the interface,

$$J(p, x, y) = I_0(p) \delta(x) \delta(y), \quad (1.6)$$

where $I_0(p)$ is the Laplace transform of the total array current. We consider only the surface wave, i.e., the electric field at the interface $x = 0$. Then

$$E(p, 0, y) = 4\pi p I_0(p) G(p, 0, 0, y), \quad (1.7)$$

where

$$G(p, 0, 0, y) = \frac{1}{2(\epsilon_b - \epsilon_a)py} \times [n_a H_1^{(1)}(ipn_a y) - n_b H_1^{(1)}(ipn_b y)], \quad (1.8)$$

$H_1^{(1)}$ is the Hankel function, and $n_{a,b} \equiv n_{a,b}(p) = \sqrt{\epsilon_{a,b}(p)}$. Thus, the surface wave $E(t, 0, y)$ is expressed in terms of the total array current $I_0(t)$ by the integral equation

$$E(t, 0, y) = -2i \int_{C(x,y)} e^{pt} p G(p, 0, 0, y) \times \int_0^\infty e^{-p\tilde{t}} I_0(\tilde{t}) d\tilde{t} dp \quad (1.9)$$

or

$$E(t, 0, y) = \int_0^\infty K(t - \tilde{t}, y) I_0(\tilde{t}) d\tilde{t}, \quad (1.10)$$

where

$$K(t, y) = -2i \int_{C(y)} e^{pt} p G(p, 0, 0, y) dp. \quad (1.11)$$

Thus, the array current reconstruction by the surface wave is reduced to the solution of a linear integral convolution-type equation, i.e., to the classical ill-posed problem. It would seem that the simplest way of its solution is the calculation of the Laplace transform of the surface wave, then the calculation of the current transform by the formula (1.7), and the calculation of the original from the current transform. However, there arise problems with stabilization of the solution, since the errors of surface wave measurements (digitization error, receiver noise, and external noise) are known in the t space, and the transfer of error statistics to the p space requires significant efforts. Therefore, we formulate a stable procedure of the current reconstruction as searching for the minimum of the functional

$$\begin{aligned} \Phi(I_0()) &= \sum_{l,m} D_{l,m}^{-1} [E(t_l, 0, y_m) - E_{l,m}^{(\text{exp})}]^2 + \alpha \int_0^\infty \left(\frac{dI_0}{dt} \right)^2 dt \\ &= \sum_{l,m} D_{l,m}^{-1} \left[\int_0^\infty K(t_l - \tilde{t}, y_m) I_0(\tilde{t}) d\tilde{t} - E_{l,m}^{(\text{exp})} \right]^2 + \alpha \int_0^\infty \left(\frac{dI_0}{dt} \right)^2 dt, \end{aligned} \quad (1.12)$$

where $E_{l,m}^{(\text{exp})}$ is the field measured at the instant t_l at the point y_m and $D_{l,m}$ is the measurement error variance. The coefficient α is chosen from the condition that the second term (residual) has the same order of magnitude as the first term.

2. CURRENT PARAMETRIZATION

To be able to perform numerical minimization of functional (1.12), the function $I_0(t)$ should be parametrized by a finite number of parameters. Let the function $I_0(t)$ be continuous and vanish outside a finite interval $(0, T)$. Then it is reasonable to parametrize it in the segment $[0, T]$ by the sine-Fourier transform coefficients

$$I_0(t) = \sum_{n=1}^{\infty} a_n \sin(\omega_n t), \quad t \in [0, T], \quad (2.1)$$

where $\omega_n = n\pi/T$. At the segment ends, both basis functions and $I_0(t)$ vanish, which justifies the use of namely the sine-Fourier transform. The completeness and orthogonality of the set of basis functions (2.1) follow from the completeness and orthogonality of basis functions of the ordinary Fourier transform in the interval $[-T, T]$, if it is considered in the class of odd functions and it is taken into account that coefficients at cosine harmonics vanish for odd functions.

Now we write the Laplace transform of the basis functions equal to $\sin(\omega_n t)$ in the segment $[0, T]$ and to zero outside this segment,

$$\int_0^T e^{-pt} \sin(\omega_n t) dt = [1 - (-1)^n e^{-pT}] \frac{\omega_n}{p^2 + \omega_n^2}. \quad (2.2)$$

Substituting expressions (2.1) and (2.2) into (1.9), we obtain

$$E(t, 0, y) = \sum_{n=1}^{\infty} a_n E_n(t, y), \tag{2.3}$$

where

$$E_n(t, y) = F_n^{(a)}(t, y) - F_n^{(b)}(t, y), \tag{2.4}$$

$$F_n^{(a,b)}(t, y) = G_n^{(a,b)}(t, y) - (-1)^n G_n^{(a,b)}(t - T, y), \tag{2.5}$$

$$G_n^{(a)}(t, y) = \frac{1}{iy} \int_{C_n^{(a)}(y)} e^{pt} \frac{n_a(p)}{\epsilon_b(p) - \epsilon_a(p)} \frac{\omega_n}{p^2 + \omega_n^2} H_1^{(1)}(ipn_a y) dp, \tag{2.6}$$

$$G_n^{(b)}(t, y) = \frac{1}{iy} \int_{C_n^{(b)}(y)} e^{pt} \frac{n_b(p)}{\epsilon_b(p) - \epsilon_a(p)} \frac{\omega_n}{p^2 + \omega_n^2} H_1^{(1)}(ipn_b y) dp. \tag{2.7}$$

Substituting (2.1) and (2.3) into (1.12), we obtain

$$\Phi(a_1, a_2, \dots, a_M) = \sum_{l,m} D_{l,m}^{-1} \left[\sum_{n=1}^M a_n E_n(t_l, y_m) - E_{l,m}^{(\text{exp})} \right]^2 + \tilde{\alpha} \sum_{n=1}^M n^2 a_n^2, \tag{2.8}$$

where $\tilde{\alpha} = \alpha(\pi^2/2T^2)$. The parameter M is determined experimentally from the condition that the reconstructed current

$$I_0(t) = \sum_{n=1}^M a_n \sin(\omega_n t) \tag{2.9}$$

ceases to vary as M increases.

Thus, the current reconstruction problem is reduced to searching for the minimum of quadratic function (2.8). There are rapid and efficient procedures of numerical minimization for its solution.

3. CHOICE OF INTEGRATION CONTOURS

We enlarge on the problem of choosing the integration contours in integrals (2.6) and (2.7). It is dictated by the arrangement of integrand singularities. We further assume that the upper medium is air and set $\epsilon_a = n_a = 1$; the permittivity of the lower medium is described by the model

$$\epsilon_b(p) = \epsilon_0 + \sigma/p, \tag{3.1}$$

where σ is the medium conductivity. For this model, the singularity is at $p_s = 0$, the branch point is at $p_v = -\sigma/\epsilon_0$ [2].

In addition to the singularities $n_b(p)$, the integrands have poles at $p = \pm i\omega_n$. The Hankel function $H_1^{(1)}(z)$ is analytical in z and single-valued in the region $-\pi \leq \arg z < \pi$. Its only singularities are the points $z = 0$ and $z = \infty$. At $z \rightarrow \infty$, $H_1^{(1)}(z) \rightarrow \sqrt{2/\pi z} \exp[i(z - 3\pi/4)]$; therefore, at $p \rightarrow \infty$, the exponential factor of the integrands has the form $\exp[p(t - n_\infty y)]$, where n_∞ is unity for air and $\sqrt{\epsilon_0}$ for the lower medium. At $t < n_\infty y$, the integration contour is in the right halfplane ($\text{Re } p > 0$), where the integrands have no singularities and the integrals are zero. This means that the causality principle is satisfied in the explicit form and signal fronts move with velocity n_∞^{-1} .

When integrating over the left halfplane, the contribution of poles can be calculated by the theory of residues as

$$\tilde{G}_n^{(a,b)}(t, y) = \frac{2\pi}{y} \text{Im} \left\{ \exp(i\omega_n t) \frac{n_{a,b}(i\omega_n)}{\epsilon_b(i\omega_n) - \epsilon_a(i\omega_n)} H_1^{(1)}[-\omega_n n_{a,b}(i\omega_n) y] \right\}. \tag{3.2}$$

To account for other singularities, the contour including a circle of radius R with center at zero and a section along the real p axis in the interval $(-\infty, -R)$ is the most natural integration contour. Along this section, the integrand decreases exponentially.

When integrating the Hankel functions $H_1^{(1)}(z)$, it should be kept in mind that standard procedures calculate main branches of cylindrical functions in the range $-\pi \leq \arg z < \pi$. A corresponding section in the p plane will pass over the upper part of the imaginary axis, which breaks the necessary symmetry of sections with respect to the real axis. This can be avoided if the integrand $g(p)$ is calculated only in the lower halfplane p ; for the upper halfplane, we use the relation $g(p^*) = g^*(p)$ (the symbol $*$ means complex conjugation) which follows from the definition of the Laplace transform of real functions. Let us enlarge on this problem.

We consider the Hankel function representation in the form of the series (see [2])

$$H_m^{(1)}(z) = J_m(z) + iN_m(z), \quad (3.3)$$

$$J_m(z) = z^m \sum_{k=0}^{\infty} C_k z^{2k}, \quad (3.4)$$

$$N_m(z) = \frac{2}{\pi} J_m(z) \left(\ln \frac{z}{2} + C \right) + z^m \sum_{k=0}^{\infty} C_k^{(1)} z^{2k} + z^{-m} \sum_{k=0}^{m-1} C_k^{(2)} z^{2k}, \quad (3.5)$$

where the constants C with different indices are real coefficients. Going from z to p ($z = ip = \exp(i\pi/2)p$) and taking into account that $\ln z = \ln p + i\pi/2$, we obtain

$$N_m(p) = iJ_m(p) + i^m \tilde{N}_m(p), \quad (3.6)$$

$$H_m^{(1)}(ip) = i^{m+1} \tilde{N}_m(p) = \frac{2}{\pi} i^{-m-1} K_m(p), \quad (3.7)$$

where

$$\begin{aligned} \tilde{N}_m(p) &= \frac{2}{\pi} p^m \sum_{k=0}^{\infty} (-1)^k C_k p^{2k} \left(\ln \frac{p}{2} + C \right) \\ &+ p^m \sum_{k=0}^{\infty} (-1)^k C_k^{(1)} p^{2k} \\ &+ (-p)^{-m} \sum_{k=0}^{m-1} (-1)^k C_k^{(2)} p^{2k}, \end{aligned} \quad (3.8)$$

$\tilde{N}_m(p)$ and $K_m(p)$ are real functions at real values $p > 0$ ($K_m(p)$ is the modified Bessel function [2]). Thus, for the series representation, the integrand symmetry problem is reduced to where the section should be for the unique determination of the function $\ln z$. If, when calculating the main branch of

the Hankel function (3.2), (3.5), the section is made along the negative part of the real z axis, which corresponds to the positive part of the imaginary semiaxis p , then, when calculating the main branch of the functions $\tilde{N}_m(p)$, $K_m(p)$ (see (3.7) and (3.8)), the section should pass along the negative part of the real p axis.

In the numerical calculation of the Hankel functions, along with the series representation, asymptotic expansions at large argument values are also used. These expansions are valid at $|z| \rightarrow \infty$ in the region $|\arg z| < \pi$ [3]. It can be expected that the closer the value of $\arg z$ to $\pm\pi$, the worse the asymptotic expansion convergence. The lower halfplane p corresponds to the segment $|\arg z| \leq \pi/2$, where the asymptotic expansion convergence should be best.

Thus, in numerical calculation of the Laplace transforms, instead of Hankel functions, modified Hankel functions should be used, which are defined as

$$K_m(p) = \begin{cases} \frac{\pi}{2} i^{m+1} H_m^{(1)}(ip), & \text{Im } p \leq 0 \Rightarrow \text{Re}(ip) \geq 0, \\ K_m^*(p^*), & \text{Im } p > 0 \Rightarrow \text{Re}(ip) < 0. \end{cases} \quad (3.9)$$

For such a definition, it is clear that the condition $K_m(p^*) = K_m^*(p)$ is satisfied; if $f(p^*) = f^*(p)$, then $K_m(f(p^*)) = K_m(f^*(p)) = K_m^*(f(p))$. This suggests that integrands from (2.6) and (2.7) will also obey the required symmetry condition $g(p^*) = g^*(p)$. For the contour C symmetric with respect to the real axis,

$$G = (iy)^{-1} \int_C g(p) dp = \frac{2}{y} \text{Im} \int_{C_-} g(p) dp, \quad (3.10)$$

where C_- is a contour portion arranged in the half-plane $\text{Im } p \leq 0$. For the contour including a circle of radius R with center at zero and the section along the real p axis, in the interval $(-\infty, -R)$, we have

$$\begin{aligned} G &= \frac{2}{y} \int_{-\infty}^{-R} \text{Im}[g(p - i0)] dp \\ &+ \frac{2R}{y} \int_{-\pi}^0 \text{Re}[g(e^{i\phi} R) e^{i\phi}] d\phi. \end{aligned} \quad (3.11)$$

Let us estimate the improper integral for $R \gg \max\{\omega_n, \sigma/\epsilon_0, 1/n_\infty y\}$,

$$n_b \approx n_\infty \left(1 + \frac{\sigma}{2\epsilon_0 p} \right), \quad n_\infty = \sqrt{\epsilon_0}, \quad (3.12)$$

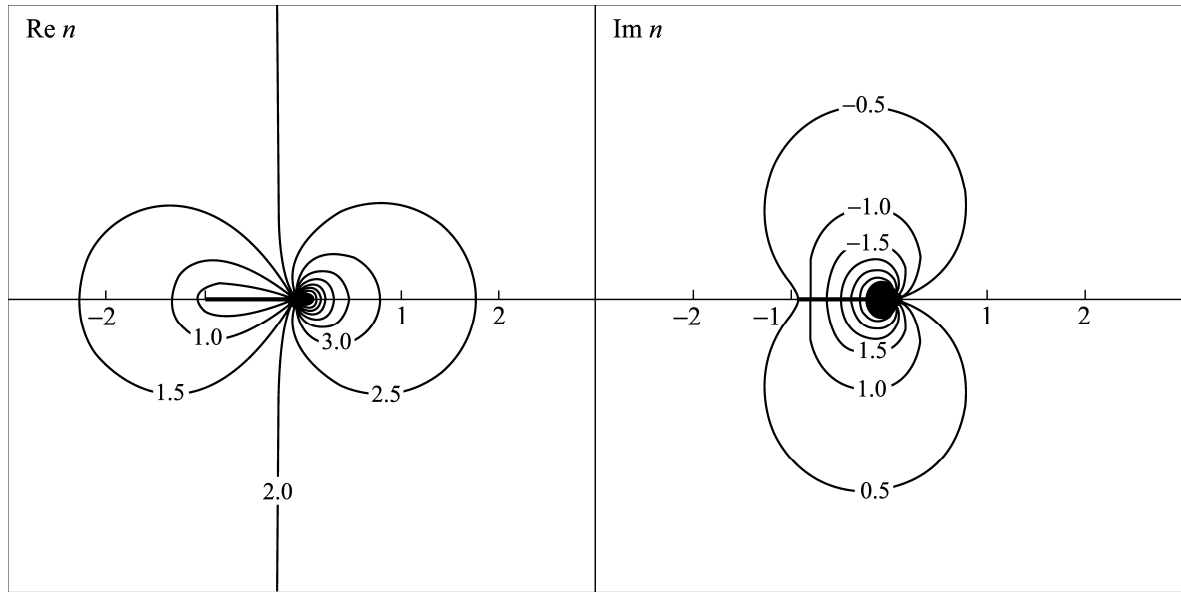


Fig. 1. Isolines of the real and imaginary parts of $n(p)$ at $\epsilon_0 = 4$ and $\sigma = 4$.

$$H_1^{(1)}(ipn_b y) \approx -i \sqrt{\frac{2}{\pi |p| n_\infty y}} \exp\left(-pn_\infty y - \frac{\sigma y}{2n_\infty}\right), \quad (3.13)$$

$$\int_{-\infty}^{-R} \text{Im}[g(p - i0)] dp \approx -\sqrt{\frac{2}{\pi n_\infty y \epsilon_0 - 1}} \frac{n_\infty \omega_n}{\epsilon_0 - 1} \exp\left(-\frac{\sigma y}{2n_\infty}\right) \int_{-\infty}^{-R} |p|^{-5/2} \exp(pt - pn_\infty y) dp. \quad (3.14)$$

To estimate the latter integral, the function

$$\int_{-\infty}^{-R} |p|^{-5/2} e^{kp} dp \approx \begin{cases} \frac{2}{3} R^{-3/2} e^{-kR}, & kR < \frac{2}{3}, \\ \frac{1}{k} R^{-5/2} e^{-kR}, & kR > \frac{3}{2} \end{cases}$$

can be used.

4. NUMERICAL CALCULATION RESULTS

To verify the program execution correctness, we used following tests.

(i) Independence of the values of the integrals in (2.6) and (2.7) from the choice of the radius R of the circle. Residues can enter the circle or be outside it.

(ii) The tendency of the values of the integrals in (2.6) and (2.7) to zero at $t - n_\infty y \rightarrow +0$.

To achieve the highest accuracy in the calculation of the integrals in (2.6) and (2.7), the radii of circles should be chosen adaptively: the larger t , the smaller R . However, preliminary estimate showed that the computational accuracy better than 10^{-7} is provided at $R = 0.05$ in the entire time interval $t < 100$ ns of our

interest. The conductivity was assumed to be sufficiently low in order that the refractive index section would be inside the circle.

Formulas (2.4) and (2.5) show that the field from each current harmonic can be written as four terms. Formula (2.5) describes the fact that the restricted sine is representable as a sum (difference) of semi-restricted sines shifted by an odd (even) number of half-periods. Formula (2.4) means that the surface wave is a sum of two waves propagating with velocities equal to wave velocities in both media separated by the surface. Figure 2 shows the stages of the surface wave formation for the first two current harmonics from initial semi-restricted signals according to the scheme described above (the value $y = 5.0$ ns corresponds to the 1.5-m distance between arrays).

Figure 3 shows the dependence of the electric field of the surface wave on the distance between the transmitter and receiver for two different current profiles in the transmitter array. The permittivity corresponds to distilled water. We can see how the surface wave splits into waves moving with velocities corresponding to air and water.

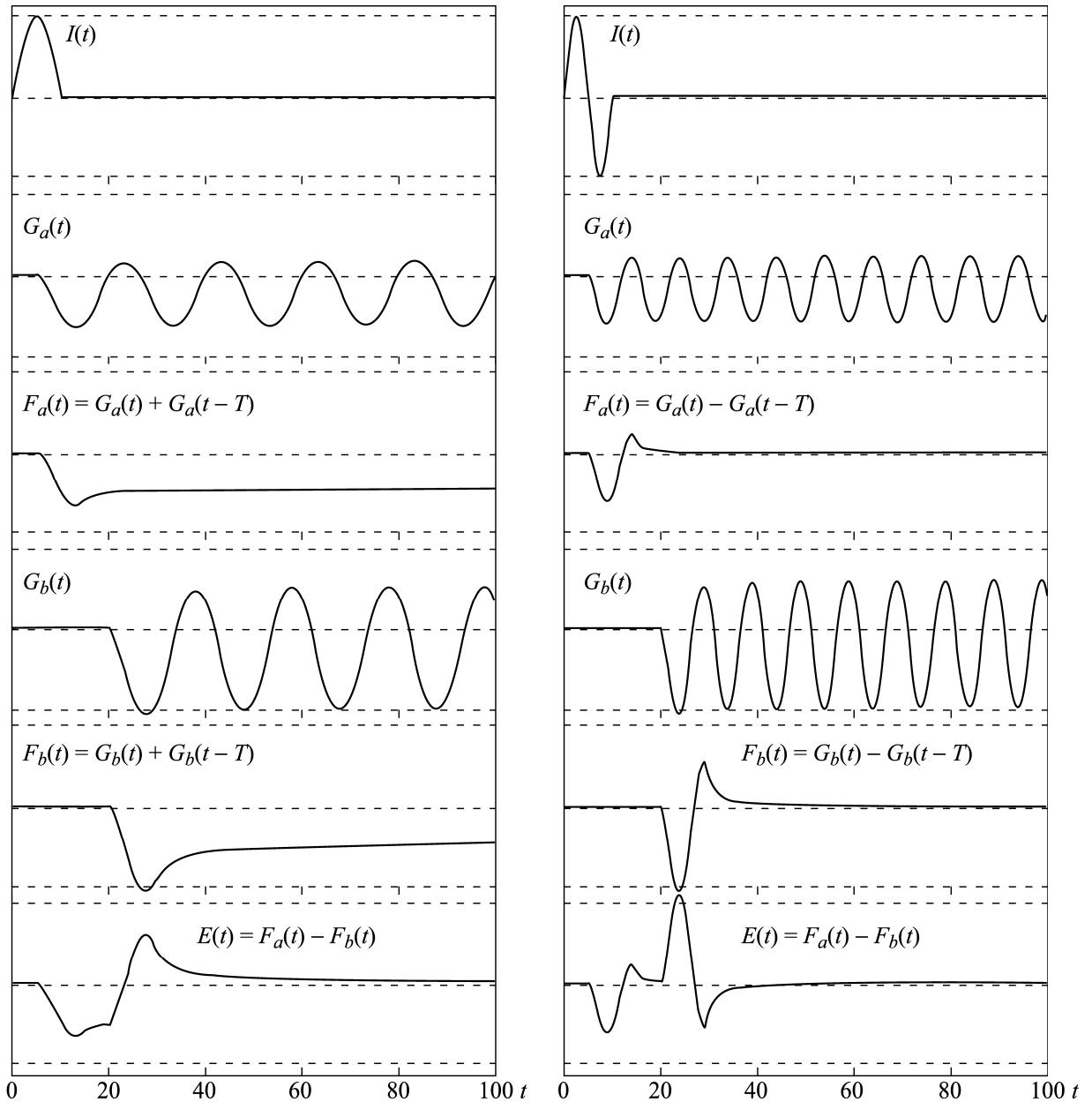


Fig. 2. Stages of surface wave formation at $\epsilon_0 = 16$, $\sigma = 0.01$, $T = 10$, and $y = 5.0$.

Figure 4 shows the results of current reconstruction according to the data of measurements on the water surface. The distance between arrays is $y_0 = 3.7$ ns. We can see good qualitative agreement between theory and experiment; the experimental field indeed represents a sum of two waves split according to the distance between arrays.

Figure 5 shows the reconstructed current and the signals reflected from the bottom at various depths.

For the best agreement with experimental data, the following changes were made.

(i) The integration contour was changed so that the calculation could be carried out at any conduc-

tivity, when integration contours represent two semi-circles of radius 0.05 with centers at the singularities $p=0$ and $p=-\sigma/\epsilon_0$ connected by segments parallel to the real axis.

(ii) The possibility of varying and determining the optimum measurement start time $t^{(0)}$ and conductivity σ was provided. The zero time corresponds to the current pulse onset in the array. The measurement start time is associated with the first point of the data set used in the calculation. Its number I_0 is specified manually. The files $G_n^{(a,b)}(t_l, y_m)$ were calculated on a grid $t_l \geq 0$ such that the equality

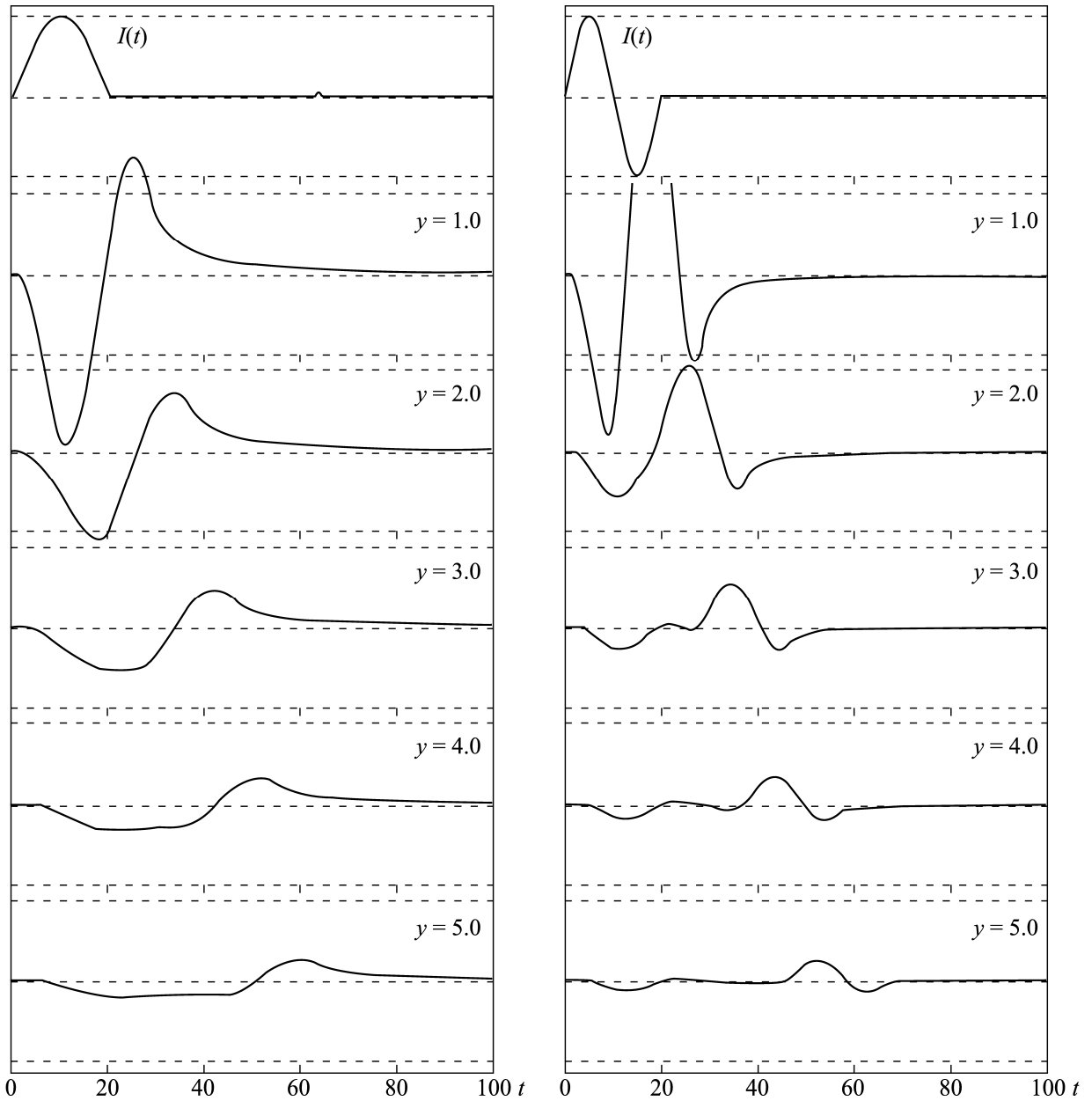


Fig. 3. Dependence of the surface wave field on the distance between arrays at $\epsilon_0 = 81$ and $\sigma = 0.01$.

$t_{L_0} = t^{(0)}$ is valid for certain L_0 . The objective function $\Psi(t^{(0)}, \sigma)$ represents values of the quadratic function $\Phi(a_1, a_2, \dots, a_M)$ (2.8) at the minimum point. The current shape is controlled by the optimization results. The optimum values were found as $y_0 = 3.9$ ns, $\sigma = 3.4378$ ns⁻¹, $t^{(0)} = 9.8920$ ns ($I_0 = 2$) (Fig. 6).

The actual distance between arrays (1.3 m) corresponds to $y_0 = 4.33$ ns. The calculated value $y_0 = 3.9$ ns corresponds to the 1.17-m distance between arrays. At $y_0 = 4.33$ ns, optimization does not make it possible to obtain reasonable current profiles (Fig. 7).

Figure 8 which was obtained at the current profile shown in Fig. 6 illustrates the disagreement between allowable and observed values of the field.

Let us now analyze the possible causes of the disagreement in the values of the parameters.

The error in the determination of the distance between arrays is excluded; hence, the first possible explanation is the frequency digitization error. If the signal digitization lies in the range of 1 ± 0.1 ns, this can lead to such disagreements.

The second explanation is that we use an overestimated value of ϵ_0 . The interval between fronts of waves propagating in air and water is $(\sqrt{\epsilon_0} - 1)y_0$.

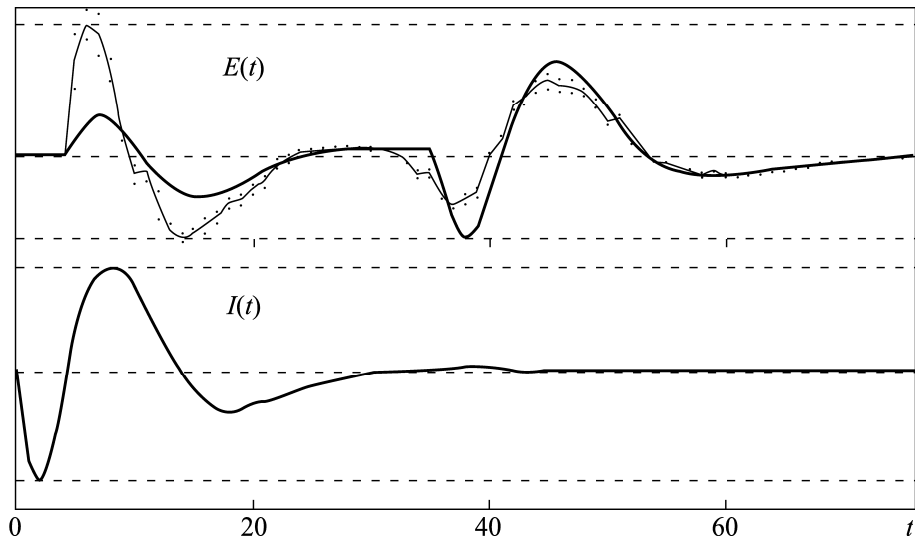


Fig. 4. Current reconstruction by measurements of the surface wave field. The thin curve (top) corresponds to experimental values of the field, dots show the measurement error, the bold curve (top) is the reconstructed field, the bold curve (bottom) is the reconstructed current; $y_0 = 3.7$ ns, $\epsilon_0 = 81$, $\sigma = 1.0$.

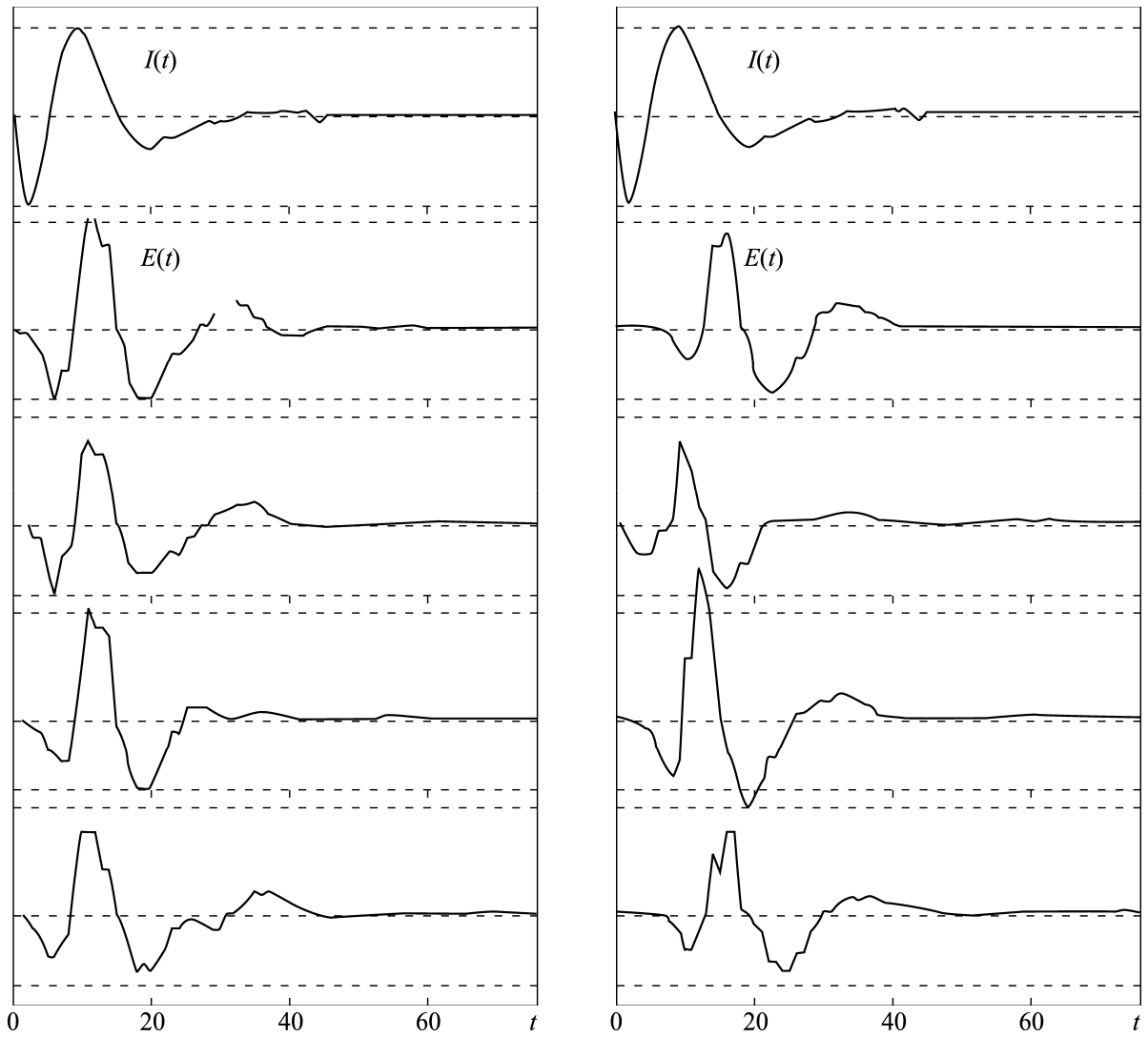


Fig. 5. Reconstructed current and signals reflected from the bottom at maximum (left) and minimum (right) bottom depths.

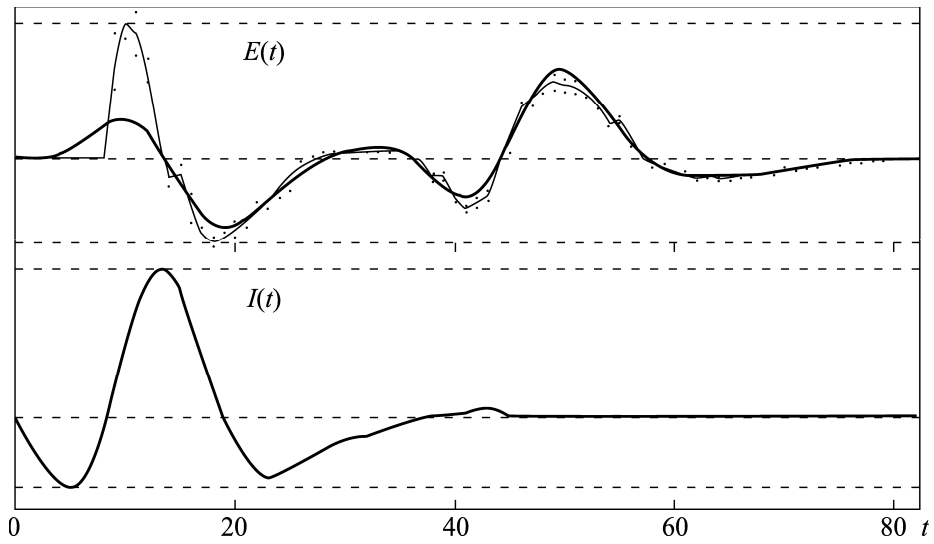


Fig. 6. Current reconstruction by measurements of the surface wave field. The thin curve (top) corresponds to experimental values of the field, dots show the measurement error, the bold curve (top) is the reconstructed field, the bold curve (bottom) is the reconstructed current; $\epsilon_0 = 81$, $y_0 = 3.9$ ns, $\sigma = 3.4378$ ns⁻¹, and $t^{(0)} = 9.8920$ ns ($I_0 = 2$).

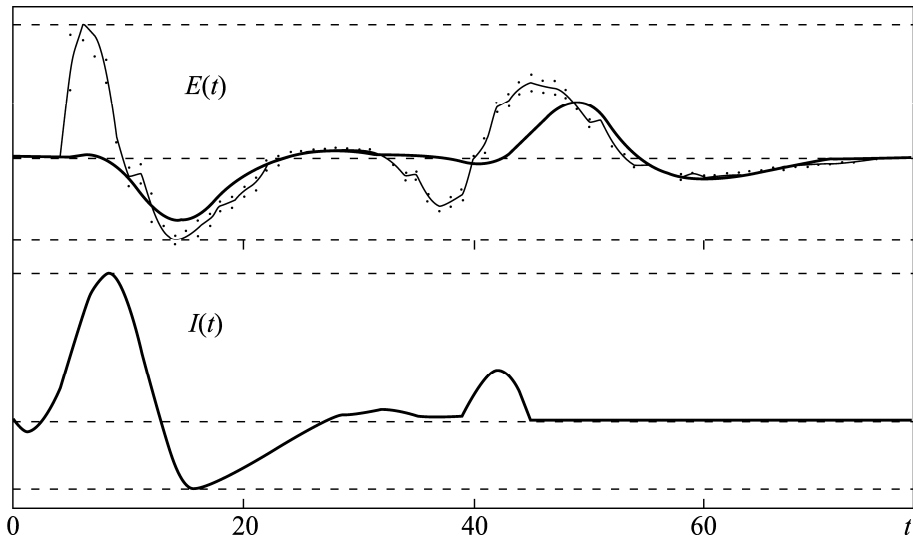


Fig. 7. The same as in Fig. 6 but for $y_0 = 4.33$ ns, $\sigma = 3.2265$ ns⁻¹, and $t^{(0)} = 5.3300$ ns ($I_0 = 2$).

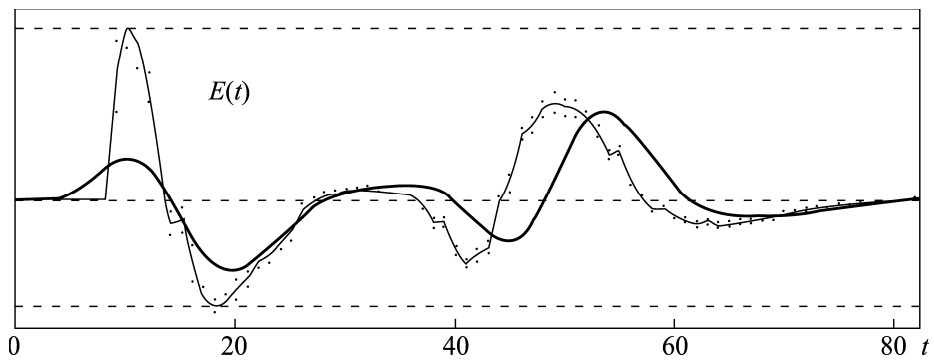


Fig. 8. The same as in Fig. 6 but for $y_0 = 4.33$ ns, $\sigma = 3.4378$ ns⁻¹, and $t^{(0)} = 9.8920$ ns ($I_0 = 2$). The current $I(t)$ is the same as in Fig. 6.

At $\sqrt{\epsilon_0} = 9$ and $y_0 = 3.9$ ns, this interval is 31.2 ns; at $y_0 = 4.33$ ns, it is equal to ~ 34.6 ns. Thus, the wave propagating in water comes earlier by ~ 3.4 ns than it follows from the simplest theoretical estimate, and this advance is clearly seen in Fig. 8. However, this contradiction can be eliminated by setting $\sqrt{\epsilon_0} = 8.2$, which corresponds to $\epsilon_0 = 67$. Certainly, the value $\epsilon_0 = 81$ for distilled water at frequencies lower than the orientation polarization frequency cannot be in doubt. Even at the minimum orientation polarization frequency $\alpha = 10^{10}$ Hz [1] (the signal period $T = 20$ ns), its contribution to the real part of the permittivity cannot exceed $4\pi^2/(\alpha T)^2 \approx 0.1\%$. At the same time, the water conductivity in the experiment under consideration is approximately 30 times larger than the distilled water conductivity; the consideration of inertia of charge carrier particles results in a decrease in the real part of the permittivity [1].

The third and most probable explanation is as follows. The receiver operation in the GROT georadars is synchronized by the transmitter pulse, which allows referencing the digitization frequency to the leading edge of the sounding pulse while retaining the structural independence of the transmitter and receiver [4]. The synchronization level is controlled by the noise level. Therefore, the sounding pulse profile can be experimentally varied by synchronization.

5. CONCLUSION

Thus, this study allows one to solve the inverse problem of current reconstruction for the two-dimen-

sional approximation. Despite some quantitative disagreements, the solution can be constructed for rapid data processing in georadar sounding.

REFERENCES

1. E. A. Rudenchik, L. B. Volkomirskaya, and A. E. Reznikov, "Investigation of the Propagation of Signals in One-Dimensional Electrodynamics for Interpreting Electromagnetic Sounding Data. Consideration of the Analytic Properties of Permittivity," *Phys. Wave Phenom.* **16**(1), 52 (2008).
2. E. A. Rudenchik, L. B. Volkomirskaya, and A. E. Reznikov, "Study of Signal Propagation in One-Dimensional Electrodynamics for Interpreting Electromagnetic Sounding Data. Consideration of Conductivity in the Function of Permittivity," *Phys. Wave Phenom.* **16**(2), 105 (2008).
3. G. A. Korn and T. M. Korn, *Mathematical Handbook for Scientists and Engineers* (McGraw-Hill, N.Y., 1968).
4. L. B. Volkomirskaya, V. V. Varenkov, A. N. Lobzina, V. V. Lobzin, A. E. Reznikov, and E. A. Rudenchik, "Main Features in the Design of GROT-10 and GROT-11 Georadars, Experience of their Operation and Data Processing," in *Problems of Subsurface Radiolocation* (Radiotekhnika, Moscow, 2005), p. 246 [in Russian].